Applied Catalysis B: Environment and Energy 367 (2025) 125099

Contents lists available at ScienceDirect

Applied Catalysis B: Environment and Energy

journal homepage: www.elsevier.com/locate/apcatb

Spatial confinement effect of zeolite Silicalite-1 on dispersing high loading Cu nanoparticles and their superior ethanol dehydrogenation catalytic performance

Yanfei Zhang [a,b,**,1], Haocheng Hu [b,c,1], Zeyu Yang [a,1], Shiping Liu [b], Tingshu Yang [a], Linying Wang [b], Yiming Sun [a], Xiaofeng Wang [a,*], Qingbo Li [a], Peng Tian [b,*]

[a] Green Shipping and Carbon Neutrality Lab, College of Environmental Science and Engineering, Dalian Maritime University, Dalian 116026, China
[b] National Engineering Research Center of Lower-Carbon Catalysis Technology, Dalian Institute of Chemical Physics, Chinese Academy of Sciences, Dalian 116023, China
[c] University of Chinese Academy of Sciences, Beijing 100049, China

ARTICLE INFO

Keywords:
Cu nanoparticles-encapsulated Silicalite-1 zeolite
High metal loading
Spatial confinement effect
Ethanol dehydrogenation
Kinetics

ABSTRACT

Ethanol dehydrogenation process contributes significantly to the ethanol-based chemical industry which is expected to grow up in the forthcoming future. Cu-based catalysts are highly active for this process, while the poor stability of which limits its practical application. Encapsulating Cu species into zeolites exhibits great potential in creating and stabilizing Cu nanoparticles. The present investigation reports the synthesis of Cu@Silicalite-1 (Cu@S-1) catalysts with high Cu loading up to 10 wt% and finely distributed nanoparticles of 2.5–5 nm by a modified steam-assisted strategy. Cu@S-1 presents robust and stable catalytic performance for the dehydrogenation of ethanol to acetaldehyde, remarkably superior to Cu/SiO_2. No aggregation of Cu species could be observed after three cycles of harsh reaction-oxidative regeneration-reductive activation or long-term reaction. Kinetic investigation reveals that the rates of ethanol dehydrogenation exhibit a Langmuir dependence on ethanol partial pressure. The rate coefficient for rate-limiting C-H cleavage over Cu@S-1 is about 2.4 times higher than that over Cu/SiO_2 at 523 K, in consistency with its superior dehydrogenation performance. Furthermore, Cu@S-1 possesses lower apparent activation energy and ethanol adsorption enthalpy compared with Cu/SiO_2. *In situ* infrared and X-ray photoelectron spectroscopy investigation prove that the Cu@S-1 catalyst with rich amount of Cu^+ is kinetically favorable for ethanol dehydrogenation.

1. Introduction

Direct ethanol (EtOH) dehydrogenation to acetaldehyde (AcH) and hydrogen is an attractive alternative way for AcH production which currently mainly relies on the Wacker oxidation of non-sustainable ethylene route over expensive palladium catalyst [1–8]. Concerning the continuously increasing production of EtOH, development of efficient EtOH dehydrogenation to AcH technique would contribute to the EtOH-based chemical industry that is anticipated to make a significant growth in the forthcoming future. In 2018, the bio-EtOH production surpassed 30 billion gallons with an increase of ca. 5 % for the next several years. Besides, the world first zeolite-catalyzed dimethyl ether (DME) carbonylation unit was commercialized in 2017 for EtOH production, which is growing rapidly in China and by 2025 [9], the total production capacity will reach around 4 million tons, with an industrial value of around 36 billion USD [10].

One of the most famous cases for the utilization of AcH in industry is the production of 1,3-butadiene from the Ostromislensky process, once industrialized in Russia in 1900s, by co-conversion of EtOH and AcH over Lewis-acid-base centers through consecutive processes including aldol condensation, Meerwein-Ponndorf-Verley (MPV) reduction and dehydration reactions [11–23]. Besides the manufacture of 1,

* Corresponding authors.
** Corresponding author at: Green Shipping and Carbon Neutrality Lab, College of Environmental Science and Engineering, Dalian Maritime University, Dalian 116026, China.
E-mail addresses: yfzh920@dlmu.edu.cn (Y. Zhang), wangxf@dlmu.edu.cn (X. Wang), tianpeng@dicp.ac.cn (P. Tian).
[1] Contributed equally

https://doi.org/10.1016/j.apcatb.2025.125099
Received 3 December 2024; Received in revised form 23 January 2025; Accepted 24 January 2025
Available online 25 January 2025

3-butadiene as bulk commodity chemicals, AcH as raw material can also react with NH_3, Cl_2, HCN, ROH as well as formaldehyde to produce a wide range of fine chemicals.

Transition metals (Ag, Zn, Zr, Ni and Cu) supported materials have been widely investigated for EtOH dehydrogenation reaction [24–28]. Based on previous investigations, both metal species and the support impose remarkable influence on their EtOH dehydrogenation activity and selectivity [29–32]. Up to now, Cu supported over non-acidic siliceous material exhibits high catalytic activity as well as selectivity, which is regarded as one of the promising catalyst [33,34]. Construction of Cu nanoparticles with high dispersion and accessibility is important for obtaining active EtOH dehydrogenation catalyst. However, as Cu possesses a low Tamman temperature (678 K), the Cu nano-clusters/particles, especially with higher concentration, will undergo migration and coalescence, aggravating the Ostwald ripening to generate large-size Cu particles, and causing the deactivation of catalyst [35,36]. Consequently, one of the major challenges for the utilization of Cu-based siliceous catalysts is enhancing the catalyst stability while maintaining its high activity and selectivity.

Cheng et al. found that the metal and support interaction (B-O-Cu^+ linkages) could prevent the Cu species from aggregating [37]. Compared with introducing Cu over amorphous silica (SiO_2) support, encapsulating the Cu species into microporous crystalline zeolite during the zeolite synthesis process exhibits great potential in creating and stabilizing nano-sized Cu species, since the confined zeolite cavities or channels could provide spatial restriction and improve the metal stability against sintering during catalysis [38,39]. Confining noble metals like Pt, Rh and the corresponding bimetallic centers in microporous zeolite crystals have been well demonstrated for propane dehydrogenation, which is generally performed at high temperature of $>$ 823 K [40–42]. However, reports for the encapsulation of non-noble metal species with high loading and uniform nano-scale size into zeolites are still limited. Besides the geometrical confinement advantage in stabilizing metal species, it is found that encapsulation of metal species into zeolites would further generate metal-support interaction (MSI), promoting the generation of oxidative metal species [43,44]. Despite the recognition of essential valence for Cu active sites remains controversial, Cu species with oxidative states play a critical role in the efficient conversion of EtOH to AcH [1,37,45–47]. Zheng et al. proposed that $Cu^{\delta+}$ ($1 < \delta < 2$) species formed due to the strong interaction between Cu and MFI support are the essential active centers for EtOH dehydrogenation [38]. Accordingly, a (Cu/MFI)@MFI catalyst with theoretical Cu loading of 5 % via secondary growth of MFI zeolite shell over Cu/MFI precursor was synthesized, which exhibits well stability for AcH generation in about 190 h time on stream [39]. The size of Cu particles within (Cu/MFI)@MFI was estimated to be ca. 19 nm. Luo and co-workers confined ultra-small and finely distributed Cu nanoparticles (~1.8 nm) inside Silicalite-1 (S-1) via in-situ hydrothermal synthesis strategy [1], where tetraethylenepentamine was applied as protecting agent for Cu^{2+} cations and the Cu loading was limited to around 2 wt%. Styskalik et al. tried four different pathways to prepare Cu/SiO_2 catalysts with ~2.5 wt% of Cu [48]. The Cu species size can be modified from sub-nanometer clusters with hydrolytic sol−gel method to large particles up to 32 nm with dry impregnation method. Based on the recent investigations, achievements have been obtained in the construction of well-distributed Cu nanoparticles by utilizing zeolite supports, however, it is still challenging to fabricate high concentration ($>$ 5 wt%) of Cu species with finely distributed nano-scale size in zeolites through a one-step and cost-effective synthesis process.

To achieve the goals proposed above, herein, we report a steam-assisted strategy for embedding high concentration of nano-scaled Cu particles in zeolites. The synthesis involves the use of pre-fabricated metal phyllosilicate (AE-Cu-SiO_2) as precursor, delivering metal nanoparticles-encapsulated Silicalite-1 (Cu@S-1) with high metal loading of 4–10 wt% and finely distributed nanoparticles of 2.5–5 nm (depends on the metal loading amounts). The prepared Cu@S-1 catalysts presented high AcH formation rate and long-term stability in the EtOH dehydrogenation to AcH reaction, remarkably superior to conventional Cu/SiO_2 catalyst. Kinetic measurements and detailed characterization were further carried out to reveal the intrinsic reaction activity of the catalysts and the reaction mechanism. Pseudo *in situ* X-ray photoelectron spectroscopy characterization revealed the essential oxidation state of Cu active sites over Cu@S-1 is + 1. Kinetic experiment showed that Cu@S-1 presented relatively lower apparent activation energy (62.2 kJ/mol) compared with Cu/SiO_2 (68.2 kJ/mol) and the rate coefficient of EtOH dehydrogenation over Cu@S-1 is around 2.4 times higher than that over Cu/SiO_2. It is well demonstrated that the spatial confinement effect of zeolite framework prevents the sintering of Cu nanoparticles and facilitates the preservation of intrinsically active Cu^+ species, which is kinetically favorable for EtOH dehydrogenation.

2. Experimental methods

2.1. Catalyst synthesis

2.1.1. Synthesis of AE-Cu-SiO_2 precursor

The AE-Cu-SiO_2 precursor for Cu@S-1 synthesis was prepared by an ammonia evaporation (AE) method. Typically, certain amounts of Cu $(NO_3)_2{\cdot}3\ H_2O$ was dissolved in 250 mL of deionized water and subsequently, 13 mL of 25 % ammonia aqueous solution was added within 30 min under agitation. Then, 12.0 g of fumed silica was added into the formed copper ammonia complex solution. After stirring for 4 h at 308 K, the temperature was rapidly increased to 363 K to allow for the complete evaporation of ammonia and the deposition of copper species onto the silica. After the pH of the suspension decreased to 6–7, the generated precipitate was filtered, washed with deionized water and dried at 393 K overnight. The synthetic precursors were calcined in static air at 723 K for 4 h, pelletized, crushed, sieved to 20–40 meshes. Through varying the amount of $Cu(NO_3)_2{\cdot}3H_2O$, AE-Cu-SiO_2 precursors with different Cu weight loadings were prepared and denoted as xAE-Cu-SiO_2, where x stands for the weight percent of Cu.

2.1.2. Synthesis of Cu@S-1

Cu@S-1 zeolites were synthesized by a steam-assisted crystallization method using AE-Cu-SiO_2 as precursor. Firstly, 1.3 g of AE-Cu-SiO_2 was impregnated with 25 % tetrapropylammonium hydroxide (TPAOH) aqueous solution. Then, the gel was dried at 323 K to remove excess water, forming a dry gel with a composition of n Cu: 1.0 SiO_2: 0.25 TPAOH: 7.0 H_2O. Subsequently, the dry gel was transferred to a Teflon plate and sealed in a Teflon-lined stainless-steel autoclave with 10 mL water at the bottom of the autoclave. After crystallization at 423 K for 3 days, the solid was collected by filtration, washed with deionized water, dried overnight at 353 K and finally calcined in air at 823 K for 4 h to remove organic species. The products were labeled as yCu@S-1, where y means the weight percent of Cu (y = 4 wt%, 8 wt% and 10 wt%, respectively).

2.1.3. Synthesis of Cu/SiO_2

Cu-supported silica (Cu/SiO_2) catalysts were prepared for comparison via wetness impregnation method. Typically, certain amounts of Cu $(NO_3)_2{\cdot}3H_2O$ was dissolved in a minimum amount of water (10.0 g) to obtain the target Cu weight loadings. 2.8 g of the solution was then added dropwise into the silica support (1.0 g) to get a uniform gel. After impregnation, the gel was subsequently dried at room temperature for more than 24 h and 323 K for 0.5 h to remove excess water. This step was followed by further heating the dry material to 673 K at rate of 2 K/min and holding it at this temperature for 4 h under static air, after which it was cooled to room temperature. The black products obtained were denoted as zCu/SiO_2, where z means the weight percent of Cu (z = 4 wt % and 8 wt%, respectively). To explore the influence of calcination conditions, Cu/SiO_2 with Cu loading amount of 8 wt% was also prepared following similar calcination process as that utilized for Cu@S-1, which

is denoted as 8 wt%Cu/SiO_2-HT.

2.2. Catalyst characterization

The Cu contents in the Cu@S-1 and Cu/SiO_2 catalysts were determined using inductively coupled plasma optical emission spectroscopy (ICP-OES). Powder X-ray diffraction (XRD) patterns were acquired on X′pert Pro diffractometer equipped with a Cu-Kα source (60 kV, 55 mA). To obtain the textural properties of catalysts, N_2 physisorption-desorption isotherms were acquired at liquid nitrogen temperature (77 K) using a gas adsorption analyzer (Micrometrics 3Flex). Temperature programmed reduction of H_2 (H_2-TPR) was performed to investigate the redox property of catalyst. Specifically, about 100 mg of calcined catalyst was loaded into a quartz tube and dried in argon stream at 423 K for 1 h to remove the adsorbed water. After being cooled down to 323 K, the catalyst was heated in 10 %H_2/Ar at a heating rate of 10 K/min up to 873 K and the TCD signal was recorded.

To observe the morphologies and crystal sizes of catalysts, scanning electron microscopy (SEM, Hitachi SU8020) was performed. Transmission electron microscopy (TEM) and energy dispersive spectroscopy (EDS) mapping were used to characterize the dispersion of metal species, crystalline structure and elemental distributions of the catalysts. In order to distinguish the distribution of metal species, a combination of focused ion beam/scanning electron microscopy (FIB/SEM) slicing with TEM imaging techniques was applied. The sample was firstly thinned to a thickness of less than 100 nm through FIB sectioning on a FEI Helios 5CX FIB/SEM system and then observed under a JEM-ARM200F transmission electron microscope. To assess the coke generation during EtOH reaction, thermogravimetry (TG) analysis of fresh, reduced and spent catalysts were carried out with SDT Q600 thermal analyzer. The TG experiments were performed in the temperature range of 303 −1173 K with a heating rate of 10 K/min.

To reveal the intrinsic chemical state of Cu species during reaction, calcined and reductive pretreated catalysts were characterized by pseudo *in situ* X-ray photoelectron spectroscopy (XPS) on a Bruker Vextex 70 spectrometer equipped with a mercury-cadmium-telluride (MCT) detector. Specifically, Cu 2p and LMM XPS spectra of calcined Cu@S-1 and Cu/SiO_2 were firstly collected and then, catalysts were transferred to a pretreatment cabinet under vacuum. Subsequently, the catalysts were heated at 2 K min^{-1} from room temperature to 573 K and held at that temperature for 2 h under flowing 10 %H_2/90 %N_2, and then cooled naturally. The reductive treatment conditions mimic that for catalytic performance evaluation. After that, Cu 2p and LMM XPS spectra of reduced Cu@S-1 and Cu/SiO_2 catalysts were collected. Binding energy (BE) values were referenced to the C 1 s core level at 284.6 eV.

To investigate the evolution of intermediates, comparative analysis of EtOH conversion over Cu@S-1 and Cu/SiO_2 was performed through *in situ* Fourier transform infrared (FTIR) spectroscopy measurements using a Brukers Optics XF808–04 spectrometer. For these experiments, around 10 mg of catalyst was pressed into a thin self-supporting wafer, transferred into the transmission IR cell, and pretreated at 573 K for 2 h in 30 mL min^{-1} of 10 %H_2/90 %N_2. Subsequently, the sample was purged with 30 mL min^{-1} N_2 and cooled naturally down to reaction temperature to collect the background spectrum. After that, EtOH was fed onto the catalyst through a saturated bubbler at 283 K and 80 mL min^{-1} of flowing N_2. The spectra for EtOH conversion were recorded at constant time intervals to monitor the generation of intermediates and products.

2.3. Catalyst evaluation

EtOH conversion was performed using a fixed bed instrument equipped with a tubular quartz plug flow reactor at atmospheric pressure. Catalyst samples (~20 mg) were placed at the center of the quartz reactor and supported by a quartz wool plug. Catalyst charges less than 20 mg were diluted with SiO_2 (Silica Flash 150 A). Prior to experiments, catalysts were heated at 10 K min^{-1} from ambient temperature to 573 K under flowing 10 %H_2/90 %N_2 (30 mL min^{-1}) and held at this temperature for 2 h. Initially, the influence of pretreatment atmosphere was explored, in which N_2 was applied in place of 10 %H_2/90 %N_2 while the pretreatment temperature remains unchanged. In a typical experiment, EtOH was introduced into the stream of flowing N_2 using a syringe pump (EPP010) and N_2 was used as carrier gas. Products streams were analyzed by gas chromatography using a Panna Pro60 GC fitted with a Plot-Q capillary column and flame ionization detector.

3. Results and discussion

3.1. Synthesis and characterization of Cu@S-1 catalysts

A one-pot steam-assisted crystallization strategy is developed for the synthesis of Cu nanoparticles encapsulated in zeolite Silicalite-1 (Cu@S-1). Scheme 1 illustrates the synthetic procedures of the materials, which involves the utilization of AE-Cu-SiO_2 as a precursor. High-resolution transmission electron microscopy (TEM) characterization reveals that ultra-small CuO*x* nanoparticles (average diameter of ca. 2.5 nm) are highly dispersed in the calcined AE-8 %Cu-SiO_2 precursor (Fig. S1), which should greatly contribute to the successful encapsulation of well-dispersed metal nanoparticles in zeolites [49,50]. Moreover, Cu/SiO_2 reference catalysts were prepared via wetness impregnation method by utilizing the commercial mesoporous silica as support and to probe the relationship between the distribution of Cu species and their catalytic performance for EtOH dehydrogenation reaction.

Fig. 1A shows the XRD patterns of the calcined Cu@S-1 and Cu/SiO_2 with different Cu loadings as well as the spent catalysts after harsh catalytic evaluation and regeneration treatment. Standard XRD patterns of Silicalite-1 zeolite, Cu, Cu_2O and CuO were also shown for comparison. Accordingly, the XRD patterns of Cu@S-1 (4 wt%Cu@S-1, 8 wt% Cu@S-1 and 10 wt%Cu@S-1) present characteristic diffraction peaks of the MFI structure and the sharp peaks suggest the high crystallinity of these materials. No peaks attributable to Cu, Cu_2O and CuO species can be observed, indicating that Cu species are highly dispersed on Cu@S-1. In sharp contrast, two major peaks at 2θ values of 35.3° and 38.9° are detected for calcined Cu/SiO_2, which changed to 43.5° and 50.3° after H_2 reduction. This suggests the formation of large CuO and Cu particles over calcined and reduced Cu/SiO_2, respectively.

The Cu loadings, textural properties as well as the morphology of Cu@S-1 and Cu/SiO_2 were further characterized. In all cases, the Cu amounts on the catalysts closely matched the targeted loadings of Cu introduced (Table 1). The scanning electron microscopy (SEM) images with high and low magnification (Fig. 1C and S2) show that Cu@S-1 has a typical morphology of MFI-type zeolite with smooth surface and no bulk metal oxide particles are observed. The particle size of zeolite crystals is about 200–300 nm. N_2 physisorption-desorption isotherms of the catalysts were shown in Fig. 1B. Cu@S-1 samples have large N_2 uptakes at relative pressures below 0.01 due to the filling of micropores, which also confirms the high crystallinity of Cu@S-1 samples. Cu/SiO_2 samples show a type IV isotherm with hysteresis loop in the range of P/P_0 = 0.65–0.90 due to capillary condensation in mesopores. The detailed textural properties of these samples are summarized in Table 1. The micropore surface areas and micropore volumes of both 4 wt% Cu@S-1 and 8 wt%Cu@S-1 are ~250 m^2 g^{-1} and 0.13 cm^3 g^{-1}, respectively, which are close to those previously reported for MFI zeolite [39,51–53]. The lower values observed for 10 wt%Cu@S-1 should be attributable to the partial pore plugging caused by high concentration of metal nanoparticles. The external surface areas of Cu@S-1 are about 120–140 m^2 g^{-1}, which is in agreement with their nano-sized crystallites. For Cu/SiO_2 samples, they possess large external surface of around 154–203 m^2 g^{-1} and mesoporous volume of 0.94–1.01 cm^3 g^{-1}, but nearly no microporosity.

TEM tests were further applied for characterizing the dispersion of Cu species over SiO_2 and embedded within Silicalite-1. The major

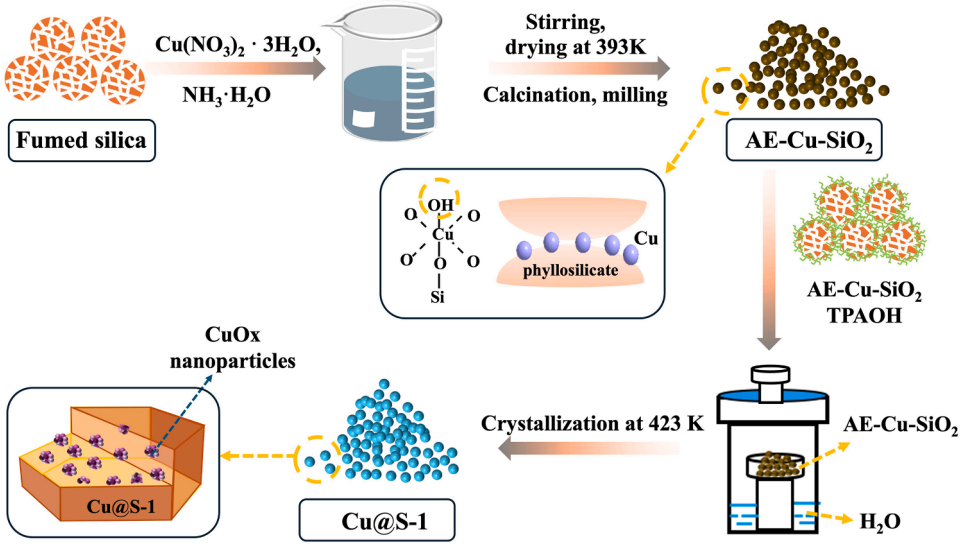

Scheme 1. Schematic illustration for the synthesis of Cu@S-1 catalysts.

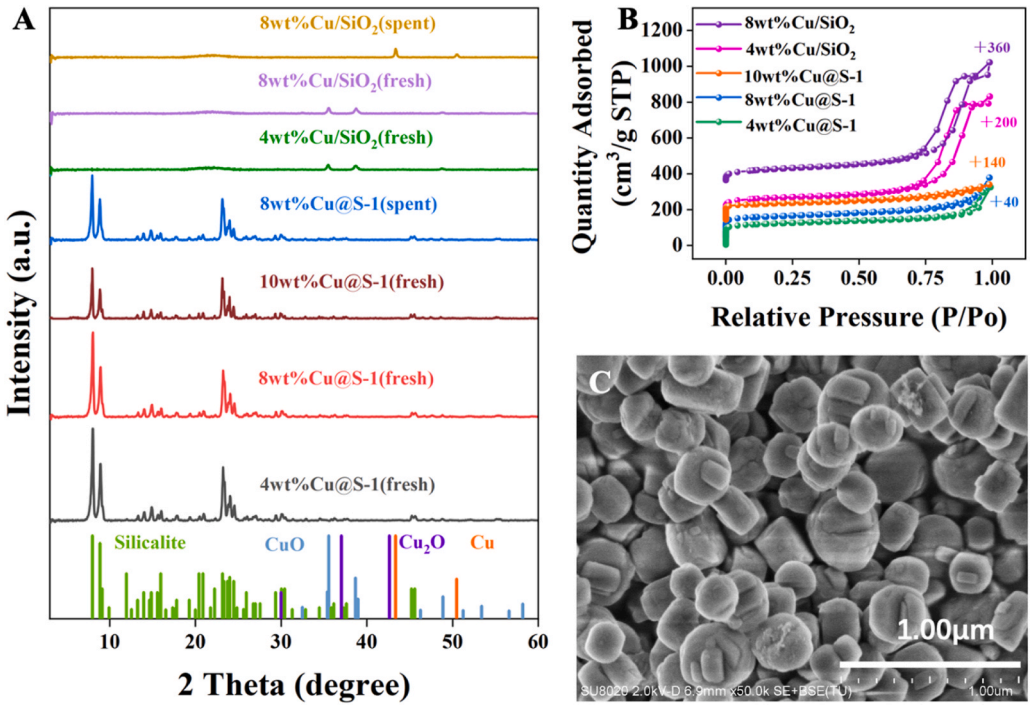

Fig. 1. (A) XRD patterns of calcined Cu@S-1 and Cu/SiO_2 catalysts with different Cu loadings as well as the spent 8 wt%Cu@S-1 and 8 wt%Cu/SiO_2 catalysts collected after reaction. (B) N_2 adsorption-desorption isotherms of Cu@S-1 and Cu/SiO_2 catalysts with different Cu loadings. (C) SEM image of calcined 8 wt%Cu@S-1 catalyst.

disadvantage of TEM is that the two-dimensional mode allows all metal species, not only metal species embedded in crystals, can be imaged. To investigate the intracrystalline distribution of metal species at high spatial resolution, a combination of focused ion beam (FIB) with TEM techniques, known as FIB/TEM slice and view, was utilized. Consecutive thin slices of the entire Cu@S-1 crystals perpendicular to the crystal substrate were collected and a high-resolution TEM image of this exposed cross-section of the crystal is recorded, as shown in Fig. 2A. It is observed that finely distributed CuO*x* nanoparticles with a dominant size of 2.5 nm are well embedded in the crystals of calcined 8 wt% Cu@S-1. No CuO*x* particles are observed on the external surface of zeolite crystals. The size distribution of CuO*x* nanoparticles is in good consistence with that of calcined AE-8 %Cu-SiO_2 precursor (Fig. S1). Fig. 2B further presents the TEM image of 8 wt%Cu@S-1 after reductive treatment, which shows that the size of Cu nanoparticles increases to 4.2 nm in comparison with its calcined counterpart. However, for the reduced 8 wt%Cu/SiO_2, obviously large Cu particles are observed with a dominant size of 54.6 nm, in line with the XRD result in Fig. 1A. These results demonstrate the effectiveness of the present synthesis strategy for encapsulating high concentration of metal nanoparticles inside the zeolite crystals. According to the previous works [54,55], the steam-assisted crystallization may follow an *in situ* dissolution-recrystallization mechanism. The SiO_2 of AE-Cu-SiO_2 precursor are activated, rearranged and *in situ* transformed to the

Table 1
Textural properties and metal loadings of Cu-based catalysts.

Catalyst	Cu loading, wt%	Surface area (m^2/g)			Pore volume (cm^3/g)	
		S^a_{BET}	S^b_{micro}	S^c_{ext}	V^d_{total}	V^e_{micro}
4 wt%Cu@S−1	4.7	391	254	137	0.50	0.15
8 wt%Cu@S−1	7.4	392	252	140	0.53	0.15
10 wt%Cu@S−1	9.8	303	182	121	0.31	0.11
4 wt%Cu/SiO_2	4.4	222	68	154	0.98	0.04
8 wt%Cu/SiO_2	6.7	237	34	203	1.03	0.02

a: S_{BET} is the total surface area obtained by Brunauer-Emmet-Teller (BET) method; b: S_{micro} is the *t*-plot micropore surface area; c: $S_{ext} = S_{BET} - S_{micro}$; d: V_{total} is the total pore volume at $P/P_0 = 0.99$; e: V_{micro} is the *t*-plot micropore volume.

framework of Silicalite-1 zeolite. The close interactions between ultra-small CuO*x* particles and SiO_2 matrix (the formation of Si-O-Cu linkages) should help the successful encapsulation of metal nanoparticles during the transformation, avoiding the occurrence of phase separation.

TEM images of reduced 4 wt%Cu@S-1 and 10 wt%Cu@S-1 are shown in Fig. 2D–E. Well-dispersed Cu nanoparticles encapsulated in crystals are observed for 4 wt%Cu@S-1, the corresponding size distribution histogram of which shows a dominant diameter of around 2.4 nm. For 10 wt%@S-1, relatively larger Cu nanoparticles (dominant diameter: ~5.2 nm) are formed. Although most of the Cu nanoparticles are embedded in the crystals, small amounts of nanoparticles are presented on the surface of crystals likely because of the high concentration of Cu species. Accordingly, Cu@S-1 with high Cu loadings up to 10 wt% and nano-scale Cu diameter of about 2.4–5.2 nm are successfully fabricated through steam-assisted crystallization method.

H_2-TPR measurement was performed to gauge the reducibility of Cu species incorporated in Silicalite-1 zeolite and that supported on SiO_2 (Fig. 3A). No obvious reduction peak is observed at temperature higher than 550 K on Cu@S-1, which indicates the complete reduction of reducible Cu species by 550 K. Beyond that, reduction of possible residual $Cu^{\delta+}$ species cannot be realized via increasing temperature. As reported for Cu/MCM-22, the assignment of reduction peak at around 473–573 K is complicated with high Cu loading, which covers the reduction of Cu^{2+} to Cu^+ and also CuO to Cu^0. Combining the XPS result shown below, the strong peak centered at 484 K of Cu@S-1 are possibly attributable to the reduction of Cu^{2+} to Cu^+ and also CuO to Cu^0 species, while the small shoulder at higher temperature (525 K) may correspond to small amounts of Cu^+ to Cu^0 species (18.5 %). For Cu/SiO_2, higher reductive temperatures are observed due to the lower accessibility of highly aggravated Cu particles by H_2 molecules. The obviously large proportion of high-temperature peak at 558 K (around 61 %), associated with the reduction of bulk CuO species and Cu^+ to Cu^0, is consistent with the larger CuO particles on Cu/SiO_2.

Pseudo in situ XPS analysis was employed to reveal the chemical state of Cu species on 8 wt%Cu/SiO_2 and 8 wt%Cu@S-1 before and after reductive treatment. Fig. 3B shows the main and the satellite peaks of Cu $2p_{3/2}$ and Cu $2p_{1/2}$ of the catalysts. The calcined 8 wt%Cu@S-1 shows Cu $2p_{1/2}$ and Cu $2p_{3/2}$ signals centered at around 956 eV and 936 eV,

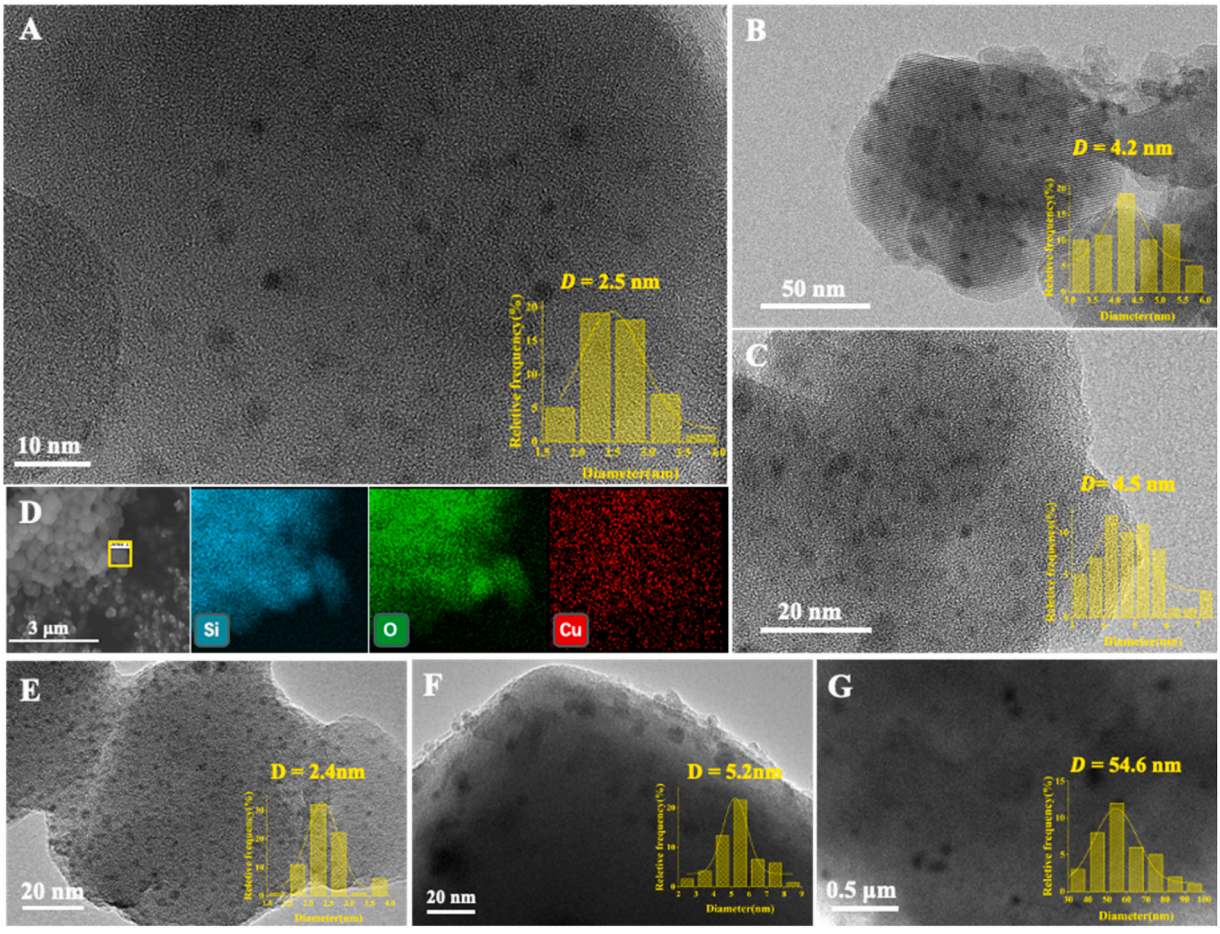

Fig. 2. High-resolution TEM images of (A) calcined 8 wt%Cu@S-1 slice sample prepared by focused ion beam slicing technique, (B) reduced 8 wt%Cu@S-1 and (C) spent 8 wt%Cu@S-1 catalyst collected after three reaction-oxidative regeneration-reductive activation cycles. (D) SEM image and elemental mapping of Si, O and Cu for reduced 8 wt%Cu@S-1 catalyst. (E-G) TEM images of reduced 4 wt%Cu@S-1, 10 wt%Cu@S-1 and 8 wt%Cu/SiO_2, respectively. The insets are the particle size distribution histograms of Cu species.

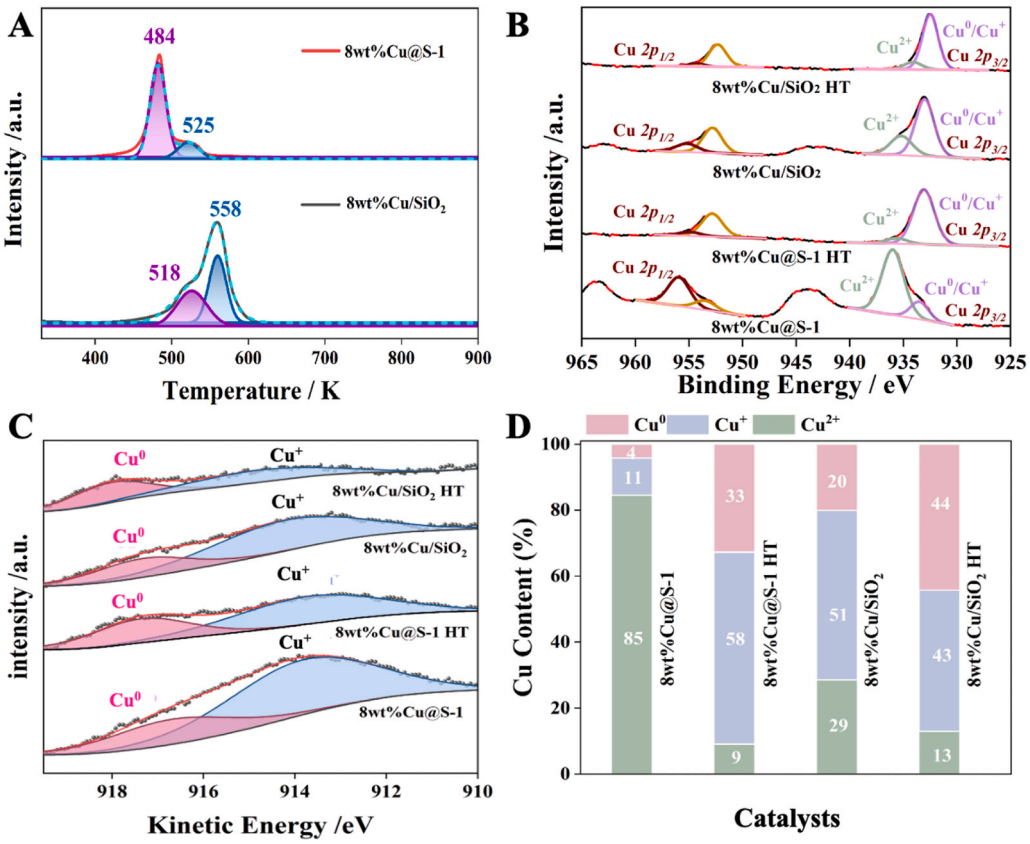

Fig. 3. (A) H_2-TPR profiles of calcined 8 wt%Cu@S-1 and 8 wt%Cu/SiO_2. (B) Cu 2p and (C) Cu LMM XPS spectra of 8 wt%Cu@S-1 and 8 wt%Cu/SiO_2 before and after H_2 reduction. (D) Cu species distribution on the calcined and reduced catalysts. Cu@S-1 HT and Cu/SiO_2 HT are corresponding catalysts after pretreatment under 10 %H_2/90 %N_2 at 573 K for 2 h.

respectively, accompanied with two strong shake-up satellite peaks situated at 943.7 eV and 962.9 eV attributable to Cu^{2+} [39,46,56]. While, calcined 8 wt%Cu/SiO_2 exhibits two signals at relatively lower binding energy (BE) of 952.8 eV and 932.9 eV and two weak satellite peaks of Cu^{2+}. Deconvolution of Cu $2p_{3/2}$ peaks was performed to clarify the content of Cu species with different valence [39,57]. The Cu^{2+} species content on calcined 8 wt%Cu@S-1 (85 %) is markedly higher than on calcined 8 wt%Cu/SiO_2 (29 %) (Fig. 3D). The existence of more Cu^{2+} species with higher BE on 8 wt%Cu@S-1 should be due to the smaller particle size of Cu species and their stronger interaction with zeolite framework [38]. After H_2 treatment, the Cu $2p_{3/2}$ peak associated with Cu^{2+} species becomes negligible, suggesting the reduction of Cu^{2+}. Quantitative analysis reveals that the content of Cu^{2+} decreases to about 9 % for 8 wt%Cu@S-1 and 13 % for 8 wt%Cu/SiO_2, respectively.

To distinguish Cu^0 and Cu^+ species, X-ray induced Auger electron spectroscopy (XAES) measurements were performed on the catalysts. As shown in Fig. 3C, two peaks centered at 916.7–918 eV and 913.6–914.4 eV attributable to reduced Cu^0 and Cu^+ species [58], respectively, were detected for all catalysts. The contents of different Cu species were estimated based on the areas of characteristic signals obtained through peak deconvolution of Cu 2p and LMM XPS spectra (Fig. 3D). It is noteworthy that the abundance of Cu^+ on 8 wt%Cu@S-1 HT catalyst (58 %) is significantly greater than that of 8 wt%Cu/SiO_2 HT (43 %), as illustrated in Fig. 3D. The predominance of Cu^+ specie on 8 wt%Cu@S-1 may be attributed to the stabilization of silanol groups of zeolite, which have been documented to effectively anchor transition metal species in zeolite-confined environments [59,61–63].

The catalytic performance of Cu@S-1 catalysts in the EtOH dehydrogenation to AcH reaction was investigated at 523 K under high weight-hourly space velocity (WHSV) of 24 h^{-1} (Fig. 4A). As shown, all catalysts are active for the reaction, and the principle carbon-based product observed is AcH. The side products include ethylene, diethyl ether (DEE) and trace amounts of ethyl acetate (EA) (Fig. 4B). 10 wt% Cu@S-1 exhibited the highest initial EtOH conversion of about 59 % and a high selectivity toward AcH (96 %). It is noted that the EtOH conversion over 10 wt%Cu@S-1 gradually drops from 59 % to 49 % in 250 min, which is possibly ascribed to the slight aggregation of some Cu nanoparticles dispersed on the external surface of zeolite with such high metal concentration. This deduction can also be verified by the superior catalytic stability and high EtOH conversion (52 %) for EtOH dehydrogenation over 8 wt%Cu@S-1 catalyst. The rate of AcH formation normalized by the amount of Cu species over 8 wt%Cu@S-1 is around 1.3 times of that over 10 wt%Cu@S-1 (Fig. 4C). Reference catalyst 8 wt %Cu/SiO_2 with the same metal loading as that of 8 wt%Cu@S-1 exhibits a remarkably lower EtOH conversion of around 36 %, which should be ascribed to the lower dispersion of Cu species as well as the lower concentration of Cu^+ active sites as proposed by Zheng et al [39]. Furthermore, a gradual deactivation can be observed for 8 wt%Cu/SiO_2. This result is consistent with previous observations that the zeolite support could provide a spatial confinement effect to disperse and stabilize metal nanoparticles encapsulated and enhance their catalytic activity due to the generation of Si-O-M linkages. To clarify the effect of calcination conditions on the distribution and catalytic performance of Cu species, 8 wt%Cu/SiO_2-HT prepared at high temperature of 823 K was also investigated for EtOH dehydrogenation under identical reaction conditions. As shown in Fig. S3A, extremely low EtOH conversion of 2 % is observed, which is remarkably lower than that on 8 wt%Cu/SiO_2. Due to the low Tamm temperature of metallic Cu and the absence of spatial restriction from support, serious Cu aggregation on 8 wt% Cu/SiO_2-HT occurs as observed in TEM image (Fig. S3B), which reduce the accessibility of Cu active sites and lead to poor catalytic activity.

To clarify the valence of intrinsic Cu active sites, the activity and

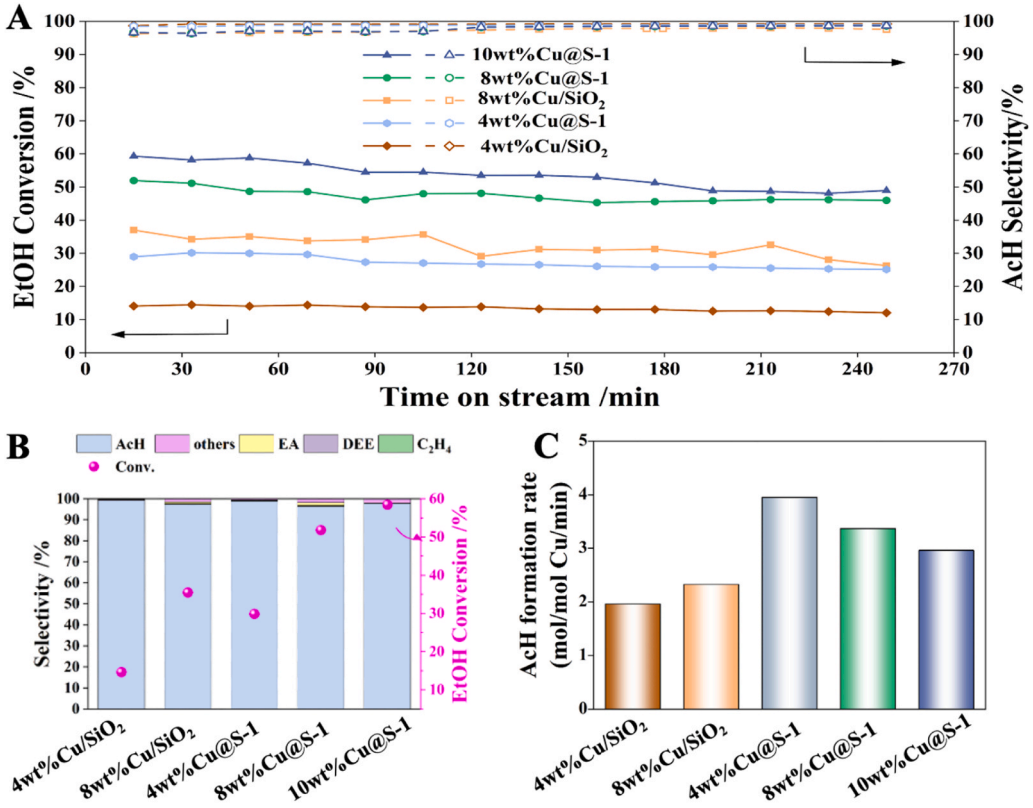

Fig. 4. (A) Conversion of EtOH and selectivity toward AcH over Cu@S-1 and Cu/SiO_2 measured at 523 K with 7.7 kPa EtOH/N_2 and WHSV= 24 h^{-1}. The average (B) products distribution and EtOH conversion as well as (C) AcH formation rates over different catalysts. Reaction conditions: EtOH flow rate = 0.6 mL/h, N_2 flow rate = 50 mL/min, m_{cat} = 0.02 g.

selectivity of 8 wt%Cu@S-1 after pretreatment in N_2 (without H_2 reduction), was also investigated for EtOH dehydrogenation. As revealed in Fig. S4, a high initial EtOH conversion of 49 %, close to that of reduced 8 wt%Cu@S-1 (52 %), can be observed. However, the conversion of EtOH decreases monotonically with time, in sharp contrast with the superior stability of reduced 8 wt%Cu@S-1 (Fig. 4A). Accordingly, it is assumed that Lewis acidic Cu^{2+} species may promote the cascade condensation of AcH to produce long-chain unsaturated aldehydes, which lead to the coverage of active sites and their deactivation. To evidence such deduction, the formation rates of coke species over spent catalysts pretreated under N_2 and H_2/N_2 atmosphere were comparatively investigated by thermogravimetry (TG) analysis. As revealed, the rate of coke formation over Cu@S-1 pretreated under N_2 is around 4.51 mg/(g·h), which is higher than that over the counterpart pretreated in reductive atmosphere (3.89 mg/(g·h)).

The dependence of the rates of EtOH dehydrogenation on the metal loadings of the catalysts is illustrated in Fig. 4. The conversion of EtOH drops as the decrease of the Cu loading, while the selectivity of AcH increases. The EtOH conversion over 4 wt%Cu@S-1 is around 29 %, which is close to that over 8 wt%Cu/SiO_2 (33 %) with twice amounts of Cu supported. While the initial conversion of EtOH over 4 wt%Cu/SiO_2 decreases to 15 %, further evidencing the superior catalytic activity of Cu species encapsulated in zeolite to that supported over SiO_2 material. The rates of EtOH dehydrogenation over Cu@S-1 and Cu/SiO_2 with different metal loadings are also normalized by the molar amount of Cu species (Fig. 4C). As shown, the dehydrogenation rates over Cu/SiO_2 normalized by this way are independent with the loading amount (2.1 mol/mol Cu/min), which may suggest that the dispersion as well as existence status of Cu species supported over SiO_2 are almost invariant with the metal loadings. While, due to the much smaller size of Cu species over 4 wt%Cu@S-1, the rate of EtOH dehydrogenation over Cu@S-1 is about 4 mol/mol Cu/min, which is around two times of Cu/SiO_2. Combined with the characterization results presented above, we attribute the excellent catalytic activity and stability of Cu@S-1 to the better dispersion of Cu species encapsulated in zeolite and enrichment in the concentration of Cu^+ active species.

Fig. 5A shows the conversion of EtOH and selectivity toward AcH measured at 4 kPa EtOH/N_2 over 8 wt%Cu@S-1 and 8 wt%Cu/SiO_2 catalysts, as a function of reaction temperature. The EtOH conversion increased nearly monotonically while the AcH selectivity only shows a slight decrease from 100 % to 95 % as the reaction temperature increases from 453 K to 553 K. Accordingly, high temperature is favorable for the dehydrogenation of EtOH to AcH. Influence of space velocity was investigated by increasing the feeding rate while maintaining the EtOH partial pressure constant (4 kPa). Throughout the experiments (Fig. 5B and S5), the dominant product is AcH, the selectivity of which rises with the increase of space velocity, which indicates that AcH is produced as a primary product. Moreover, the rates of AcH formation rise as the space velocity increases from 2.4 to 9.5 h^{-1}. With high space velocity (short space time), the diffusion of guest molecules including EtOH, intermediates and AcH would be accelerated, which is favorable for the regeneration of active sites. Concurrently, the secondary reversible AcH hydrogenation, disproportionation of AcH to EA and cascade condensation of AcH to long-chain aldehydes/ketones are significantly inhibited at high space velocity.

To get a deep insight into the reaction mechanism, the dependence of the rates of EtOH dehydrogenation on reactant partial pressures over 8 wt%Cu@S-1 and 8 wt%Cu/SiO_2 catalysts was investigated, and the results are shown in Fig. 5C. Generally, the rate of EtOH dehydrogenation over both Cu-based catalysts is positive or nearly first order with respect to EtOH at low partial pressure and then increases further but at a much lower rate with increasing EtOH partial pressure for the range of partial pressure tested (P_{EtOH} = 2–20 kPa). At low EtOH partial pressure, it is assumed that the sites responsible for EtOH dehydrogenation are

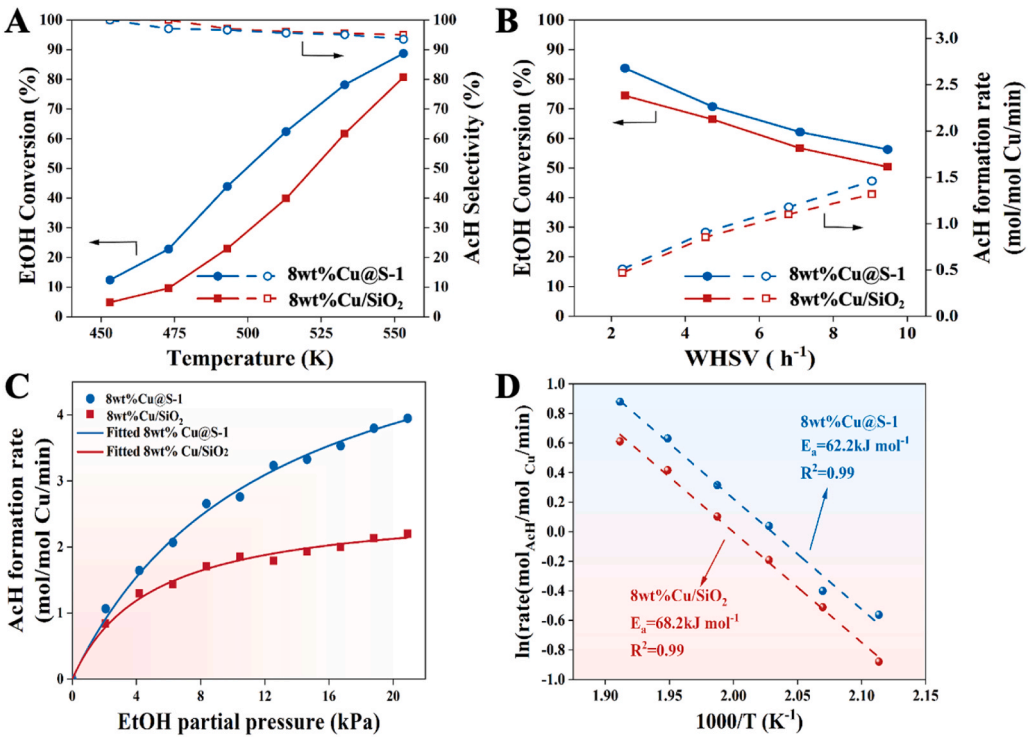

Fig. 5. (A) Effect of reaction temperature and (B) space velocity on the conversion of EtOH and selectivity toward AcH for 8 wt%Cu@S-1 and 8 wt%Cu/SiO_2. Reaction conditions of panel A: EtOH flow rate = 0.3 mL/h, N_2 flow rate = 50 mL/min, m_{cat} = 0.05 g; Reaction conditions of panel B: 523 K, EtOH flow rate = 0.3 – 1.2 mL/h, N_2 flow rate = 50 – 200 mL/min, m_{cat} = 0.1 g. (C) Effect of EtOH partial pressure on the EtOH dehydrogenation rate over 8 wt%Cu@S-1 and 8 wt%Cu/SiO_2. Reaction conditions: T = 523 K, total gas flow rate = 208 mL/min. (D) Arrhenius plots of EtOH dehydrogenation over 8 wt%Cu@S-1 and 8 wt%Cu/SiO_2. Reaction conditions: T = 473–523 K, P_{EtOH} = 4 kPa and total gas flow rate = 208 mL/min.

predominantly unoccupied, while as the partial pressure of EtOH increases, saturated adsorption of EtOH-derived species would occur, leading to a constant EtOH dehydrogenation rate. It is noted that the EtOH dehydrogenation rates approach to nearly zeroth order at a relatively lower EtOH partial pressures of about 8 kPa over 8 wt%Cu/SiO_2, indicating the saturated adsorption of EtOH-derived species. In contrast, for 8 wt%Cu@S-1, a slight bend in the rate of EtOH dehydrogenation is observed for the same range of partial pressure tested. The different behaviors regarding the influence of reactant partial pressure on EtOH dehydrogenation rates suggest weaker adsorption of EtOH over 8 wt% Cu@S-1. In this case, the adsorption of EtOH over Cu active sites is not promoted by the microporous porosity of zeolite crystals, otherwise which would lead to stronger adsorption of EtOH. Based upon the kinetics observations and the precedent for EtOH dehydrogenation in the literature [11,39,51,60], a rate expression for AcH formation from EtOH dehydrogenation can be derived using a Langmuir model and is given below in Eq. 1. The rate expression was derived with the following assumptions: the adsorption of EtOH is quasi-equilibrated; the cleavage of O-H bond of EtOH is rapid; the concentration of surficial AcH and H_2 is negligible and the C-H bond cleavage is discerned as the rate-limiting step. The assumptions and methods used to derive the rate expression are described in detail in the Supplementary Information.

$$r = \frac{kKp}{1 + Kp} \tag{1}$$

The parameter k represents the effective rate constant associated with the rate-limiting abstraction of α-H from EtOH (C-H bond cleavage), while K is the equilibrium constant for EtOH adsorption onto active sites. The rate data presented in Fig. 5C can be fitted to Eq. 1. Table 2 shows the experimentally measured rate coefficients and adsorption constants for EtOH dehydrogenation at 523 K. As estimated, the rate coefficient for EtOH dehydrogenation over Cu@S-1 is 2.4 times higher than the corresponding rate coefficient over Cu/SiO_2, which indicates obviously promoted dehydrogenation activity of Cu species confined in Silicalite-1 zeolite. In addition, the much higher equilibrium constant for EtOH adsorption on Cu/SiO_2 suggests the stronger adsorption of EtOH species, which is consistent with the phenomenon that Cu/SiO_2 is saturated by EtOH-derived species at low EtOH partial pressure. The apparent pre-exponential factors, A, were further estimated based upon the apparent activation energies and rate coefficients for EtOH dehydrogenation. As shown in Table 2, the apparent pre-exponential factor for EtOH dehydrogenation over Cu/SiO_2 is 3.3×10^6 mol/mol Cu/min, which is around 3.8 times of that over Cu@S-1. Actually, apparent pre-exponential factors are the combination of entropies of EtOH adsorption and activation, hence, it can be deduced that a small difference of 11 J/mol/K in the entropies could readily account for this small difference.

Table 2
Rate parameters for EtOH dehydrogenation over Cu@S-1 and Cu/SiO_2 measured at 523 K.

	Cu@S-1	Cu/SiO_2
rate coefficient k (mol/(mol Cu•min))	6.292	2.570
pre-exponential factor A (mol/(mol Cu•min))	8.7×10^5	3.3×10^6
EtOH adsorption constant K (kPa^{-1})	0.085	0.203

The reaction kinetics of EtOH dehydrogenation over 8 wt%Cu@S-1 and 8 wt%Cu/SiO_2 were investigated with constant EtOH partial pressure of 4 kPa. EtOH conversion was kept below 15 % (Fig. S6) to exclude the influence of surficial adsorbed products and any intermediates. From the Arrhenius plot of the rate of EtOH dehydrogenation (Fig. 5D), 8 wt% Cu@S-1 catalyst exhibited slightly lower experimental apparent activation energy of 62.2 kJ/mol than that of 8 wt%Cu/SiO_2 (68.2 kJ/mol). Taking an assumption that Cu^+ sites predominantly catalyze the rate-limiting C-H cleavage, the rates of EtOH dehydrogenation can also be

normalized per Cu^+ via dividing the rates per Cu site by the Cu^+/Cu ratio. The rates of EtOH dehydrogenation normalized this way, shown in Fig. S7, increase monotonically at low EtOH partial pressures and then increase further but at a lower rate for high EtOH partial pressures. The apparent activation energies for EtOH dehydrogenation over 8 wt%Cu/SiO_2 and 8 wt%Cu@S-1 normalized per Cu^+ active sites were estimated to be 62.9 and 68.5 kJ/mol, respectively.

As found in the effect of EtOH partial pressure on the rate of EtOH dehydrogenation above, the adsorption of EtOH over Cu nanoparticles confined in Silicalite-1 zeolite is weaker than that over larger-sized Cu particles supported on SiO_2, i.e., the adsorption enthalpy for EtOH should be less negative. On that basis, it can be reasonably deduced that the intrinsic activation energy ($E_{int} = E_{app} - \Delta H_{ads}$) for EtOH dehydrogenation over Cu@S-1 should be lower than Cu/SiO_2. This demonstrated that, besides the much higher concentration of available active centers for 8 wt%Cu@S-1, the activation barrier over 8 wt%Cu@S-1 is also lower compared with that of 8 wt%Cu/SiO_2, leading to superior dehydrogenation activity.

In situ FTIR experiments of EtOH reaction on both 8 wt%Cu@S-1 and 8 wt%Cu/SiO_2 catalysts at different temperatures were carried out to gain more insight into the surface reaction behaviors. As shown in Fig. 6 and S8, the surface hydroxyl groups over the catalysts are immediately consumed once fed in EtOH with an intense negative band at 3728 cm^{-1} for Cu@S-1 and 3740 cm^{-1} for Cu/SiO_2, because of the adsorption of EtOH over Si-OH groups. At the same time, obvious C-H stretching signals in the range of 2800–3000 cm^{-1} and C-H bending signals in the range of 1300–1500 cm^{-1} are observed, which are typical for the ethyl groups of adsorbed EtOH [64–67]. The maxima of negative IR bands are centered at 3728 cm^{-1} for Cu@S-1 and 3740 cm^{-1} for Cu/SiO_2, which are attributable to internal silanol groups in zeolitic micropores and isolated silanol groups over SiO_2, respectively [61–63]. It is also noted that the interaction between EtOH and the surface Si-OH group is weak, since the signal of Si-OH group can be easily recovered and the signals representing C-H vibration from ethyl groups of EtOH become negative once purging with N_2 for a short time of 1 min (Figs. 6B, 6D, S8B and S8D). During the EtOH reaction at 453 K, an IR band at 1723 cm^{-1} appears over Cu@S-1 (Fig. 6C), which is typical of the C═O stretching vibration in AcH [65,68]. However, no band attributable to AcH, is observed for Cu/SiO_2 even after 30 min of reaction at this temperature (453 K, Fig. S8A). As shown in Fig. S8C, further heating to 523 K reveals the appearance of weak IR band representing AcH generation at 1723 cm^{-1} for Cu/SiO_2. In sharp contrast, IR signals at 1723 cm^{-1} could be observed over 8 wt%Cu@S-1 even under much lower temperature of 423 K. These observations suggest the superior catalytic activity of Cu nanoparticles encapsulated into zeolite than Cu particles supported on SiO_2, which agrees well with the kinetics investigation that 8 wt%Cu@S-1 catalyst has much lower activation barrier for EtOH dehydrogenation reaction.

The long-term catalytic performance of EtOH dehydrogenation over Cu@S-1 and Cu/SiO_2, including activity, selectivity and durability, were comparatively investigated at 523 K (Fig. 7). Cu@S-1 shows a high initial EtOH conversion of ca. 93 % and high AcH selectivity of 88 %-99 % and undergoes extremely mild deactivation, retaining 91 % conversion even after 202 h of reaction. For Cu/SiO_2, EtOH conversion is 93 % initially and drops very rapidly to about 55 % within 37 h. Their catalytic lifetimes differ by one order of magnitude. To clarify the evolution of Cu species constructed over the catalysts during reaction, TEM images of spent catalysts were collected. For the spent 8 wt%Cu@S-1

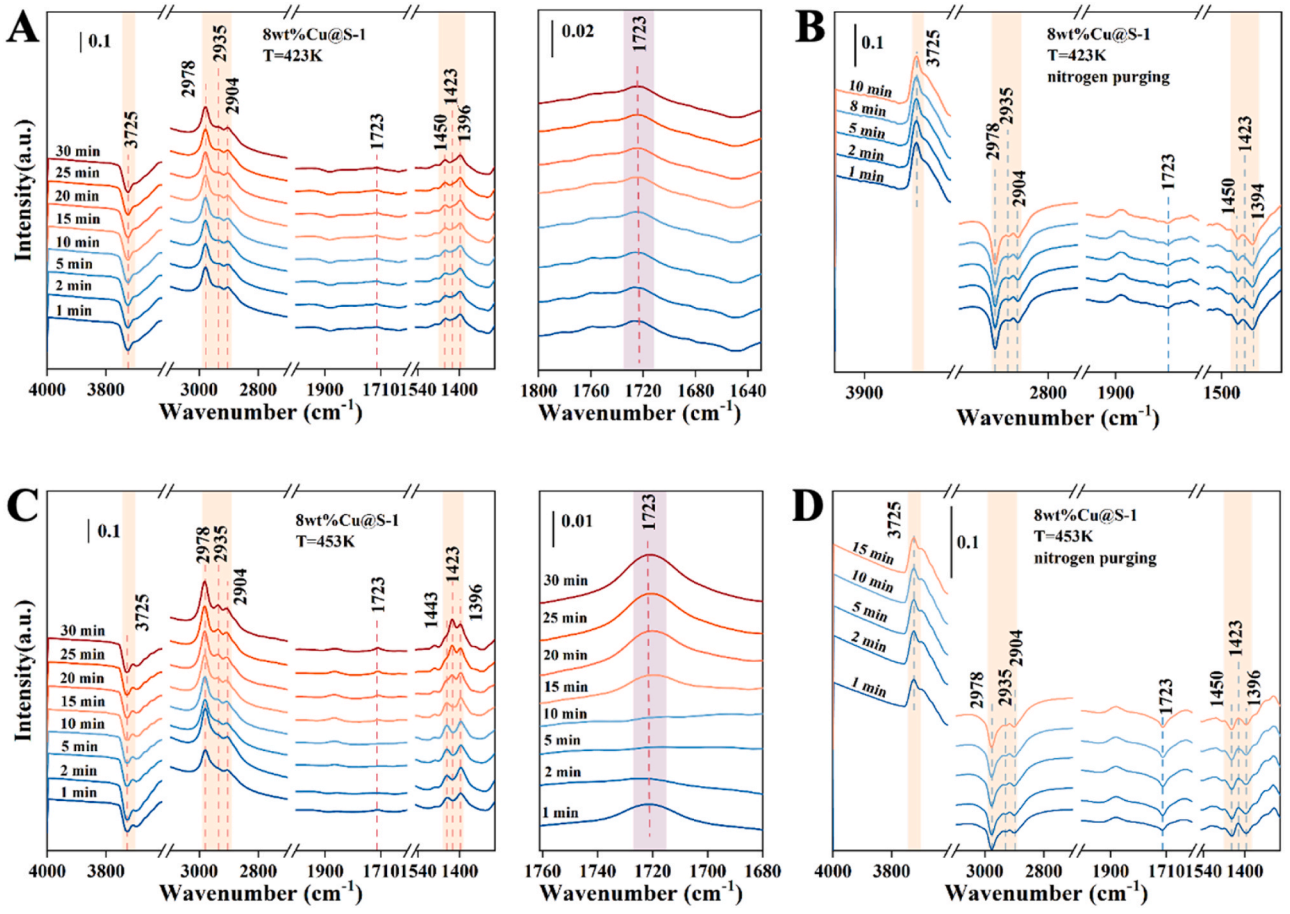

Fig. 6. In situ FTIR spectra for EtOH reaction over 8 wt%Cu@S-1 collected (A, C) during EtOH conversion and (B, D) after N_2 purging measured at 423 K and 453 K, respectively.

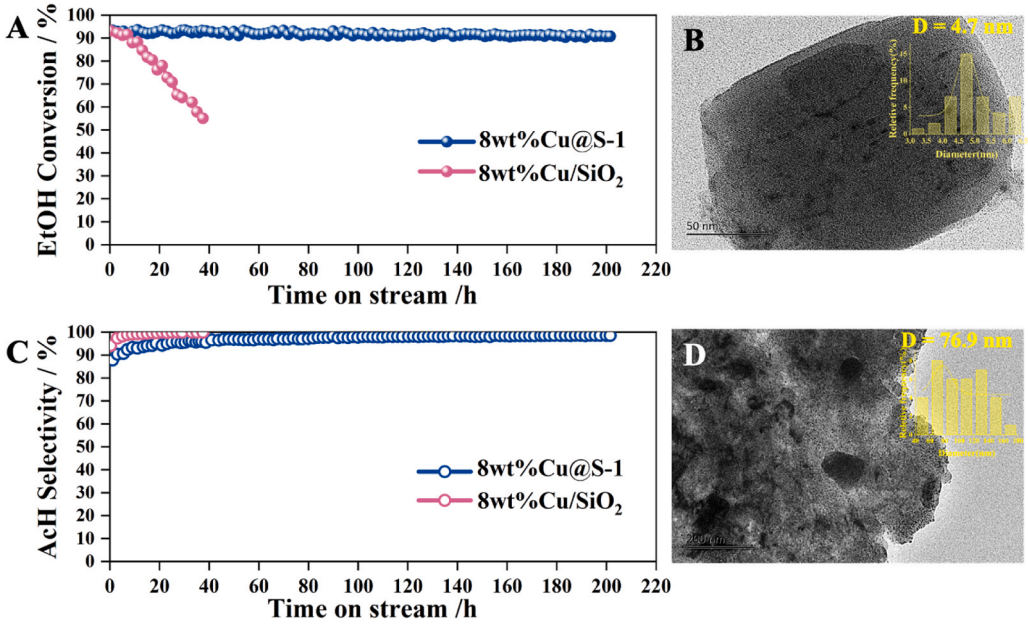

Fig. 7. (A) EtOH conversion and (C) AcH selectivity as a function of time on stream over 8 wt%Cu@S-1 and 8 wt%Cu/SiO_2 measured at 523 K with 2.5 kPa EtOH/N_2 and a space velocity of 0.53 h^{-1}. TEM images of spent (B) 8 wt%Cu@S-1 and (D) 8 wt%Cu/SiO_2 catalysts collected after long-term reaction.

catalyst (after reaction at 523 K for 202 h), Cu nanoparticles are still well dispersed in zeolite crystals with an average size of 4.7 nm (Fig. 7B), similar to what observed for fresh catalyst. In contrast, the Cu particles over 8 wt%Cu/SiO_2 further sinter and the average size increases to around 76.8 nm (Fig. 7D). The catalytic performance together with the TEM images well demonstrate that zeolite framework provides effective spatial confinement effect on stabilizing non-noble metal nanoparticles, even in reductive atmosphere. Coke deposition is generally accompanied with the EtOH dehydrogenation reaction, which may contribute to the catalyst deactivation. Thus, TG analysis of fresh, reduced and spent catalysts were performed following identical conditions, to assess the coke deposition of the spent catalyst. From Table S1 and Fig. S9, it is observed that the overall amount of coke species generated over spent Cu@S-1 after the continuous EtOH dehydrogenation reaction for 202 h is around 2.18 %, which is higher than that over spent Cu/SiO_2 catalyst after a TOS of ~40 h. Noteworthily, the formation rate of coke species estimated through dividing the coke amount by TOS is 0.30 mg/(g·h) for 8 wt%Cu/SiO_2, which is nearly 3 times faster than that over 8 wt%Cu@S-1. Therefore, 8 wt%Cu@S-1 exhibits well enhanced coke resistance in comparison with 8 wt%Cu/SiO_2. Combining the TEM and TG analysis of spent catalysts with their catalytic performance, it can be deduced that both coke deposition and Cu sintering contribute to the rapid deactivation of 8 wt%Cu/SiO_2, while slow coke generation mainly lead to the mild deactivation of 8 wt% Cu@S-1.

EtOH dehydrogenation over 8 wt%Cu@S-1 with high EtOH partial pressure of 20 kPa and high WHSV of 1.9 h^{-1} was further performed. As shown in Fig. S10, Cu@S-1 shows an initial EtOH conversion of 64 % and even after a TOS of 100 h, the EtOH conversion still remains at around 62 %, indicating its good catalytic stability. During the period, the selectivity toward AcH increases gradually from 90 % to 97 %. TEM image of the spent Cu@S-1 reveals that the dominant size of Cu species is 6.2 nm, which is slightly larger than that of the fresh catalyst (4.2 nm). Furthermore, TG analysis indicates that the formation rate of coke is 0.26 mg/(g·h), which is 2.4 times of that measured at 2.5 kPa EtOH and WHSV of 0.53 h^{-1}. Consequently, the mild deactivation of 8 wt%Cu@S-1 is caused by both enhanced coke deposition and some Cu sintering at high EtOH partial pressure.

To further evidence the spatial confinement effect of Silicalite-1 zeolite for protecting Cu species from aggregation, three continuous EtOH dehydrogenation reaction followed by air regeneration at high temperature and then H_2 pretreatment test cycles were performed for both 8 wt%Cu/SiO_2 and 8 wt%Cu@S-1 catalysts. As shown in Fig. 8, Cu/SiO_2 displays a quick deactivation after a TOS of 12 h, with a significant decrease in the EtOH conversion from 89.6 % to 76.1 %, indicating the aggregation of Cu particles. Similar deactivation of Cu/SiO_2 has also been reported by Luo et al., in which Cu/SiO_2 showed 46.5 % drop in EtOH conversion after a TOS of 16 h at even lower WHSV of 0.53 h^{-1} [1]. For 8 wt%Cu@S-1, no diminish in the EtOH conversion is observed after a TOS of 15 h under identical reaction conditions (Fig. 8B). For both Cu-based catalysts, the selectivity toward AcH gradually increases from 94 % to 99 %. Notably, 8 wt%Cu@S-1 presents very stable EtOH dehydrogenation activity and AcH selectivity even after consecutive oxidative-reductive treatment. TEM and XRD characterizing the spent Cu@S-1 sample further demonstrate the well dispersion of Cu species after reaction. The XRD pattern of spent 8 wt% Cu@S-1 (blue line, Fig. 1A) shows the characteristic peaks of MFI zeolite while no obvious peaks of Cu species can be distinguished. TEM image of spent Cu@S-1 (Fig. 2C) exhibits no changes on the Cu size and distribution compared with that of fresh sample, in good agreement with XRD result. However, for the spent Cu/SiO_2, XRD peaks at $2\theta = 43.4°$ and 50.5° attributable to metallic Cu are observed, indicating the formation of bulky Cu particles (yellow line, Fig. 1A).

The reaction mechanism for EtOH dehydrogenation to AcH over Cu@S-1 catalyst is envisioned based on the catalyst characterizations, in situ IR experiment and reaction behaviors obtained above as well as findings reported previously [33,39,64,68]. Accordingly, Cu^0 and Cu^+ confined in Silicalite-1 are both active for EtOH dehydrogenation, among which Cu^+ is reported to be the predominant active centers. *In situ* XPS experiments revealed that 58 % of Cu over reduced Cu@S-1 are presented as Cu^+ specie. Furthermore, it has been proposed that both the metal and support play critical roles in the alcohol dehydrogenation for metal supported catalysts, in which the functional groups over support generally promote the O-H cleavage and the metal sites participates in the rate-limiting C-H cleavage and H_2 recombination. As shown in Scheme 2, the mechanism starts with adsorption of EtOH with the O of hydroxyl group onto the Lewis acidic Cu^+ sites to form surface ethoxy and hydroxyl species with the assistance of Si-OH group on Silicalite-1

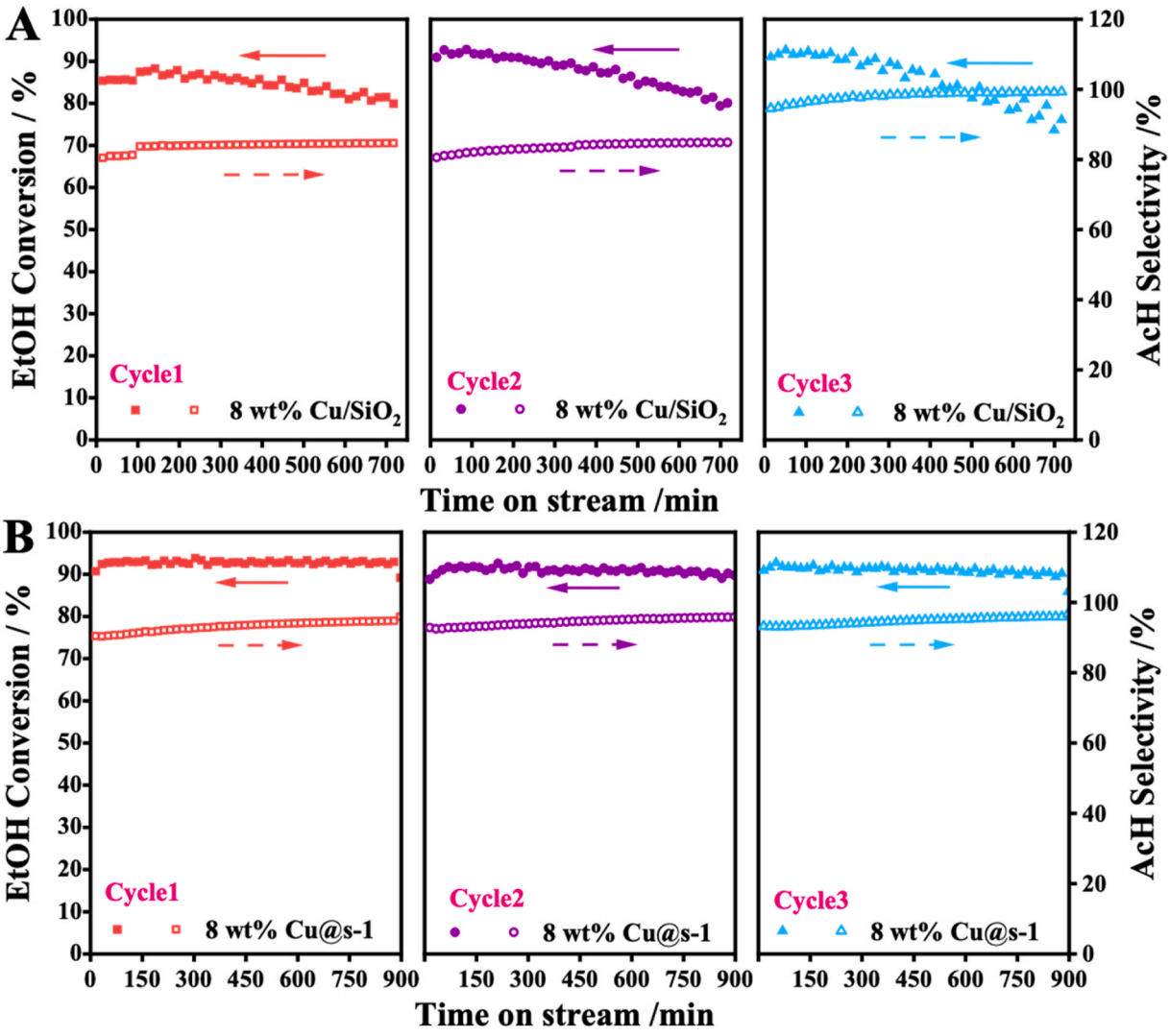

Fig. 8. Stability and regenerability of (A) 8 wt%Cu/SiO_2 and (B) 8 wt%Cu@S-1 measured at 523 K with 2.5 kPa EtOH/N_2 and a space velocity of 1 h^{-1}. Reaction conditions: EtOH flow rate = 0.126 mL/h, N_2 flow rate = 34.4 mL/min, m_{cat} = 0.1 g.

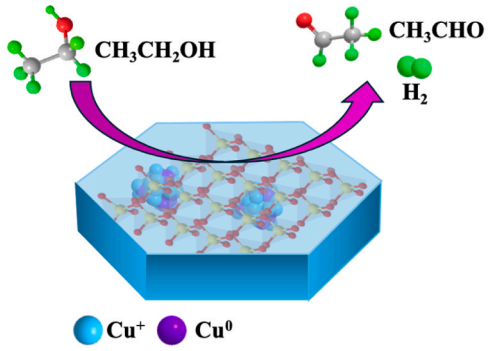

Scheme 2. Schematic illustration of reaction mechanism for EtOH dehydrogenation to AcH over Cu@S-1.

zeolite, which is confirmed by the *in situ* IR investigation of EtOH reaction (Fig. 6 and S8). This is followed by the rate-limiting C-H bond cleavage over Cu^+ sites and recombination of two H atoms to form H_2 possibly over proximal Cu^0 site.

Compared with traditional method with organic protecting agent, the steam-assisted crystallization strategy developed in this work could help create higher amounts of well-dispersed Cu species. The stronger interaction between Cu and zeolite framework O makes the Cu species more positive compared with that supported on the surface of amorphous SiO_2, and therefore leads to the lower activation barrier and superior dehydrogenation activity. More importantly, the unique confinement effect from zeolite framework can protect Cu species from sintering, providing more guarantee for catalytic stability when considering further applications.

4. Conclusion

In the present study, Cu@S-1 catalysts with high concentration of nano-scaled metal nanoparticles were successfully synthesized via utilizing metal phyllosilicates as precursor by a facile steam-assisted approach. Based on the comprehensive characterization, Cu nanoparticles were well embedded in the body of zeolite crystals. Specifically, Cu@S-1 with high loading up to 10 wt% and finely distributed nanoclusters of 2.5–5 nm were synthesized. Cu@S-1 catalyst exhibits stable catalytic performance for EtOH dehydrogenation to AcH, with an EtOH conversion of 91 % even after a TOS of 202 h at 523 K. Both the catalytic activity and stability of Cu@S-1 are superior to those of Cu/SiO_2. The regeneration ability of Cu@S-1 catalyst is evaluated under harsh conditions and no aggregation or deactivation of Cu species could

be observed, demonstrating the powerful effect of zeolite framework on preventing Cu sintering. Based on the pseudo *in situ* XPS characterization of calcined and reductive catalysts, it is proposed that the superior catalytic performance of Cu@S-1 is associated with the existence of highly active Cu^+ species and better accessibility of Cu active sites. Kinetic experiments suggest that the activity superiority of Cu@S-1 becomes more prominent with the increase of EtOH partial pressure, since the Cu/SiO_2 is more easily saturated with EtOH-derived species. The rate coefficient for EtOH dehydrogenation over Cu@S-1 is estimated to be 2.4 times higher than that over Cu/SiO_2 at 523 K.

Declaration of Competing Interest

The authors declare that they have no known competing financial interests or personal relationships that could have appeared to influence the work reported in this paper.

Acknowledgement

This work was supported by the National Natural Science Foundation of China (No. 22302025, 22288101, 21991090, 21991091, 22372170 and 22272171). Y. Z. also acknowledge support by the Fundamental Research Funds for the Central Universities of Dalian Maritime University in China (No. 3132023520).

Supplementary materials

TEM image of AE-Cu-SiO_2 precursor (Fig. S1); Low-magnification SEM image of 8 wt%Cu@S-1 catalyst (Fig. S2); Effect of calcination temperature on the catalytic performance of Cu/SiO_2 in ethanol reaction (Fig. S3); Effect of pretreatment conditions on the catalytic performance of Cu@S-1 in ethanol reaction (Fig. S4); Dependence of products distribution of ethanol conversion on WHSV (Fig. S5); Ethanol conversion as a function of reaction temperature at high WHSV (Fig. S6); Effect of ethanol partial pressure on the ethanol dehydrogenation rate normalized per Cu^+ site and Arrhenius plots of ethanol dehydrogenation over 8 wt%Cu@S-1 and 8 wt%Cu/SiO_2 (Fig. S7); In situ FTIR spectra for ethanol conversion over 8 wt%Cu/SiO_2 (Fig. S8); Thermogravimetry analysis curves of the fresh, reduced and spent catalysts (Fig. S9); Long-term investigation of the ethanol dehydrogenation measured at 20 kPa $EtOH/N_2$ and TEM image of the spent catalyst (Fig. S10); Mass change of Cu-based catalysts measured by thermogravimetry. (Table S1); Derivation of ethanol dehydrogenation rate expression.

Appendix A. Supporting information

Supplementary data associated with this article can be found in the online version at doi:10.1016/j.apcatb.2025.125099.

Data availability

The authors are unable or have chosen not to specify which data has been used.

References

[1] L. Lin, P. Cao, J. Pang, Z. Wang, Q. Jiang, Y. Su, R. Chen, Z. Wu, M. Zheng, W. Luo, Zeolite-encapsulated Cu nanoparticles with enhanced performance for ethanol dehydrogenation, J. Catal. 413 (2022) 565–574.
[2] G. Pomalaza, P.A. Ponton, M. Capron, F. Dumeignil, Ethanol-to-butadiene: the reaction and its catalysts, Catal. Sci. Technol. 10 (2020) 4860–4911.
[3] R.A. Fernandes, A.K. Jha, P. Kumar, Recent advances in wacker oxidation: from conventional to modern variants and applications, Catal. Sci. Technol. 10 (2020) 7448–7470.
[4] S. Shylesh, A. Gokhale, C. Scown, D. Kim, C. Ho, A.T. Bell, From sugars to wheels: the conversion of ethanol to 1, 3-butadiene over metal-promoted magnesia-silicate catalysts, ChemSusChem 9 (2016) 1462–1472.
[5] G. Pomalaza, M. Capron, V. Ordomsky, F. Dumeignil, Recent breakthroughs in the conversion of ethanol to butadiene, Catalysts 6 (2016) 203.
[6] D. Cespi, F. Passarini, I. Vassura, F. Cavani, Butadiene from biomass, a life cycle perspective to address sustainability in the chemical industry, Green Chem. 18 (2016) 1625–1638.
[7] R. Jira, Acetaldehyde from ethylene—a retrospective on the discovery of the wacker process, Angew. Chem. Int. Ed. 48 (2009) 9034–9037.
[8] W.C. White, Butadiene production process overview, Chem. Biol. 166 (2007) 10–14.
[9] K. Cao, D. Fan, M. Gao, B. Fan, N. Chen, L. Wang, P. Tian, Z. Liu, Recognizing the important role of surface barriers in MOR zeolite catalyzed DME carbonylation reaction, ACS Catal. 12 (2021) 1–7.
[10] J.R. Zoeller, E.M. Blakely, R.M. Moncier, T.J. Dickson, Molybdenum catalyzed carbonylation of ethylene to propionic acid and anhydride, Catal. Today 36 (1997) 227–241.
[11] L. Qi, Y. Zhang, M.A. Conrad, C.K. Russell, J. Miller, A.T. Bell, Ethanol conversion to butadiene over isolated zinc and yttrium sites grafted onto dealuminated beta zeolite, J. Am. Chem. Soc. 142 (2020) 14674–14687.
[12] G. Pomalaza, G. Vofo, M. Capron, F. Dumeignil, ZnTa-TUD-1 as an easily prepared, highly efficient catalyst for the selective conversion of ethanol to 1,3-butadiene, Green Chem. 20 (2018) 3203–3209.
[13] V.L. Sushkevich, I.I. Ivanova, Ag-Promoted ZrBEA zeolites obtained by post-synthetic modification for conversion of ethanol to butadiene, ChemSusChem 9 (2016) 2216–2225.
[14] Q. Liu, G. Xu, X. Wang, X. Mu, Selective upgrading of ethanol with methanol in water for the production of improved biofuel—isobutanol, Green Chem. 18 (2016) 2811–2818.
[15] D. Palagin, V.L. Sushkevich, I.I. Ivanova, C-C Coupling catalyzed by zeolites: is enolization the only possible pathway for aldol condensation, J. Phys. Chem. C 120 (41) (2016) 23566–23575.
[16] J.L. Cheong, Y. Shao, S.J.R. Tan, X. Li, Y. Zhang, S.S. Lee, Highly active and selective Zr/MCF catalyst for production of 1,3-butadiene from ethanol in a dual fixed bed reactor system, ACS Sustain. Chem. Eng. 4 (2016) 4887–4894.
[17] V.L. Sushkevich, A. Vimont, A. Travert, I.I. Ivanova, Spectroscopic evidence for open and closed lewis acid sites in ZrBEA zeolites, J. Phys. Chem. C 119 (2015) 17633–17639.
[18] V.L. Sushkevich, D. Palagin, I.I. Ivanova, With open arms: open sites of ZrBEA zeolite facilitate selective synthesis of butadiene from ethanol, ACS Catal. 5 (2015) 4833–4836.
[19] V.L. Sushkevich, I.I. Ivanova, E. Taarning, Ethanol conversion into butadiene over Zr-containing molecular sieves doped with silver, Green Chem. 17 (2015) 2552–2559.
[20] T. De Baerdemaeker, M. Feyen, U. Muller, B. Yilmaz, F.S. Xiao, W.P. Zhang, T. Yokoi, X.H. Bao, H. Gies, D.E. De Vos, Bimetallic Zn and Hf on silica catalysts for the conversion of ethanol to 1,3-butadiene, ACS Catal. 5 (2015) 3393–3397.
[21] P.Y. Dapsens, C. Mondelli, J. Perez-Ramirez, Design of lewis-acid centres in zeolitic matrices for the conversion of renewables, Chem. Soc. Rev. 44 (2015) 7025–7043.
[22] A. Chieregato, J.V. Ochoa, C. Bandinelli, G. Fornasari, F. Cavani, M. Mella, On the chemistry of ethanol on basic oxides: revising mechanisms and intermediates in the Lebedev and Guerbet reactions, ChemSusChem 8 (2015) 377–388.
[23] J. Sun, Y. Wang, Recent advances in catalytic conversion of ethanol to chemicals, ACS Catal. 4 (2014) 1078–1090.
[24] J. Shan, N. Janvelyan, H. Li, J. Liu, T.M. Egle, J. Ye, M.M. Biener, J. Biener, C. M. Friend, M. Flytzani-Stephanopoulos, Selective non-oxidative dehydrogenation of ethanol to acetaldehyde and hydrogen on highly dilute NiCu alloys, Appl. Catal. B Environ. 205 (2017) 541–550.
[25] K. Gao, J. Mielby, S. Kegnæs, Catalytic dehydrogenation of ethanol over zinc-containing zeolites, Catal. Today (2022) 144–151.
[26] G.V. Mamontov, M.V. Grabchenko, V.I. Sobolev, V.I. Zaikovskii, O.V. Vodyankina, Ethanol dehydrogenation over Ag-CeO_2/SiO_2 catalyst: role of Ag-CeO_2 interface, Appl. Catal. A Gen. 528 (2016) 161–167.
[27] C. Wang, G. Garbarino, L.F. Allard, F. Wilson, G. Busca, M. Flytzani-Stephanopoulos, Low-Temperature dehydrogenation of ethanol on atomically dispersed gold supported on $ZnZrO_x$, ACS Catal. 6 (2016) 210–218.
[28] R.M.M. Santos, V. Briois, L. Martins, C.V. Santilli, Insights into the preparation of copper catalysts supported on layered double hydroxide derived mixed oxides for ethanol dehydrogenation, ACS Appl. Mater. Interface 13 (2021) 26001–26012.
[29] J. Pang, M. Yin, P. Wu, X. Li, H. Li, M. Zheng, T. Zhang, Advances in catalytic dehydrogenation of ethanol to acetaldehyde, Green Chem. 23 (2021) 7902–7916.
[30] J. Ob-eye, P. Praserthdam, B. Jongsomjit, Dehydrogenation of ethanol to acetaldehyde over different metals supported on carbon catalysts, Catal 9 (2019) 66.
[31] G. Pampararo, G. Garbarino, P. Riani, M.V. García, V.S. Escribano, G. Busca, A study of ethanol dehydrogenation to acetaldehyde over supported copper catalysts: catalytic activity, deactivation and regeneration, Appl. Catal. A Gen. 602 (2020) 117710.
[32] L. He, B.C. Zhou, D.H. Sun, W.C. Li, W.L. Lv, J. Wang, Y.Q. Liang, A.H. Lu, Catalytic conversion of ethanol to oxygen-containing value-added chemicals, ACS Catal. 13 (2023) 11291–11304.
[33] H. Zhang, H.R. Tan, S. Jaenicke, G.K. Chuah, Highly efficient and robust Cu catalyst for non-oxidative dehydrogenation of ethanol to acetaldehyde and hydrogen, J. Catal. 389 (2020) 19–28.
[34] G. Pampararo, G. Garbarino, P. Riani, V. Vykoukal, G. Busca, D.P. Debecker, Ethanol dehydrogenation to acetaldehyde with mesoporous Cu-SiO_2 catalysts prepared by aerosol-assisted sol–gel, Chem. Eng. J. 465 (2023) 142715.
[35] L. Liu, J. Lu, Y. Yang, W. Ruettinger, X. Gao, M. Wang, H. Lou, Z. Wang, Y. Liu, X. Tao, Dealuminated beta zeolite reverses Ostwald ripening for durable copper nanoparticle catalysts, Science 383 (2024) 94–101.

[36] H. Liu, Z. Chang, J. Fu, Z. Hou, A CuZn-BTC derived stable Cu/ZnO@SiO_2 catalyst for ethanol dehydrogenation, Appl. Catal. B Environ. 324 (2023) 122194.
[37] S.Q. Cheng, X.F. Weng, Q.N. Wang, B.C. Zhou, W.C. Li, M.R. Li, L. He, D.Q. Wang, A.H. Lu, Defect-rich BN-supported Cu with superior dispersion for ethanol conversion to aldehyde and hydrogen, Chin. J. Catal. 43 (2022) 1092–1100.
[38] X. Li, J. Pang, Y. Zhao, P. Wu, W. Yu, P. Yan, Y. Su, M. Zheng, Ethanol dehydrogenation to acetaldehyde over a $Cu^{\delta+}$-based Cu-MFI catalyst, Chin. J. Catal. 49 (2023) 91–101.
[39] J. Pang, M. Yin, P. Wu, L. Song, X. Li, T. Zhang, M. Zheng, Redispersion and stabilization of Cu/MFI catalysts by the encapsulation method for ethanol dehydrogenation, ACS Sustain. Chem. Eng. 11 (2023) 3297–3305.
[40] L. Qi, M. Babucci, Y. Zhang, A. Lund, L. Liu, J. Li, Y. Chen, A.S. Hoffman, S.R. Bare, Y. Han, B.C. Gates, A.T. Bell, Propane dehydrogenation catalyzed by isolated Pt atoms in ≡SiOZn-OH nests in dealuminated zeolite beta, J. Am. Chem. Soc. 143 (2021) 21364–21378.
[41] L. Qi, Y. Zhang, M. Babucci, C. Chen, P. Lu, J. Li, C. Dun, A.S. Hoffman, J.J. Urban, M. Tsapatsis, Dehydrogenation of propane and n-butane catalyzed by isolated $PtZn_4$ sites supported on self-pillared zeolite pentasil nanosheets, ACS Catal. 12 (2022) 11177–11189.
[42] L. Qi, S. Das,Y. Zhang, D. Nozik, B.C. Gates, A.T. Bell, Ethene hydroformylation catalyzed by rhodium dispersed with zinc or cobalt in silanol nests of dealuminated zeolite beta, J. Am. Chem. Soc. 145 (2023) 2911–2929.
[43] D. Farrusseng,A. Tuel, Samahe Sadjadi (Ed.), Zeolite-encapsulated catalysts: challenges and prospects. Encapsulated Catalysts, Elsevier, 2017, pp. 335–386, 11.
[44] A. Rafiani, D. Aulia, G.T.M. Kadja, Zeolite-encapsulated catalyst for the biomass conversion: recent and upcoming advancements, Case Stud. Chem. Environ. Eng. 9 (2024) 100717.
[45] R. Li, M. Zhang, Y. Yu, A DFT study on the Cu (1 1 1) surface for ethyl acetate synthesis from ethanol dehydrogenation, Appl. Surf. Sci. 258 (2012) 6777–6784.
[46] M.B. Gawande, A. Goswami, F.X. Felpin, T. Asefa, X. Huang, R. Silva, X. Zou, R. Zboril, R.S. Varma, Cu and Cu-based nanoparticles: synthesis and applications in catalysis, Chem. Rev. 116 (2016) 3722–3811.
[47] M.Y. Li, W.D. Lu, L. He, F. Schüth, A.H. Lu, Tailoring the surface structure of silicon carbide support for Copper catalyzed ethanol dehydrogenation, ChemCatChem 11 (2019) 481–487.
[48] T. Pokorny, V. Vykoukal, P. Machac, Z. Moravec, N. Scotti, P. Roupcova, K. Karaskova, A. Styskalik, Ethanol dehydrogenation over copper-silica catalysts: from sub-nanometer clusters to 15 nm large particles, ACS Sustain. Chem. Eng. 11 (2023) 10980–10992.
[49] X. Dong, X. Ma, H. Xu, Q. Ge, Comparative study of silica-supported copper catalysts prepared by different methods: formation and transition of copper phyllosilicate, Catal. Sci. Technol. 6 (2016) 4151–4158.
[50] X. Kong, Y. Zhu, H. Zheng, X. Li, Y. Zhu, Y.W. Li, Ni nanoparticles inlaid nickel phyllosilicate as a metal–acid bifunctional catalyst for low-temperature hydrogenolysis reactions, ACS Catal. 5 (2015) 5914–5920.
[51] J. Pang, M. Zheng, C. Wang, X. Yang, H. Liu, X. Liu, J. Sun, Y. Wang, T. Zhang, Hierarchical echinus-like Cu-MFI catalysts for ethanol dehydrogenation, ACS Catal. 10 (2020) 13624–13629.
[52] X. Li, J. Pang, C. Wang, L. Li, X. Pan, M. Zheng, T. Zhang, Conversion of ethanol to 1,3-butadiene over high-performance Mg–ZrOx/MFI nanosheet catalysts via the two-step method, Green Chem. 22 (2020) 2852–2861.
[53] D. Dai, C. Feng, M. Wang, Q. Du, D. Liu, Y. Pan, Y. Liu, Ring-opening of furfuryl alcohol to pentanediol with extremely high selectivity over Cu/MFI catalysts with balanced Cu^0–Cu^+ and Brønsted acid sites, Catal. Sci. Technol. 12 (2022) 5879–5890.
[54] Y. Zhang, L. Xu, J. Zhang, P. Li, Y. Yuan, H. Guo, X. Zhang, L. Xu, Insight into the dissolution–crystallization strategy towards macro/meso/microporous Silicalite-1 zeolites and their performance in the Beckmann rearrangement of cyclohexanone oxime, Catal. Sci. Technol. 8 (2018) 4526–4536.
[55] Y. Zhang, P. Lu, Y. Yuan, L. Xu, H. Guo, X. Zhang, L. Xu, One pot synthesis of hierarchically macro/microporous ZSM-5 single crystals, CrystEngComm 19 (2017) 4713–4719.
[56] G. Pampararo, G. Garbarino, P. Riani, V. Vykoukal, G. Busca, D.P. Debecker, Ethanol dehydrogenation to acetaldehyde with mesoporous Cu-SiO_2 catalysts prepared by aerosol-assisted sol–gel, Chem. Eng. J. 465 (2023) 142715.
[57] J. Gong, H. Yue, Y. Zhao, S. Zhao, L. Zhao, J. Lv, S. Wang, X. Ma, Synthesis of ethanol via syngas on Cu/SiO_2 catalysts with balanced Cu^0–Cu^+ sites, J. Am. Chem. Soc. 134 (2012) 13922–13925.
[58] Y. Sun, P. Tian, D. Ding, Z. Yang, W. Wang, H. Xin, J. Xu, Y.F. Han, Revealing the active species of Cu-based catalysts for heterogeneous Fenton reaction, Appl. Catal. B Environ. 258 (2019) 117985.
[59] W. Dai, S. Zhang, Z. Yu, T. Yan, G. Wu, N. Guan, L. Li, Zeolite structural confinement effects enhance one-pot catalytic conversion of ethanol to butadiene, ACS Catal. 7 (2017) 3703–3706.
[60] S. Hanukovich, A. Dang, P. Christopher, Influence of metal oxide support acid sites on Cu-catalyzed nonoxidative dehydrogenation of ethanol to acetaldehyde, ACS Catal. 9 (2019) 3537–3550.
[61] Y. Zhang, L. Qi, A. Lund, P. Lu, A.T. Bell, Mechanism and kinetics of acetone conversion to isobutene over isolated Hf sites grafted to silicalite-1 and SiO_2, J. Am. Chem. Soc. 143 (2021) 8352–8366.
[62] Y. Zhang, L. Qi, D. Nozik, C. Dun, J.J. Urban, A.T. Bell, Mechanism and kinetics of propane and n-butane dehydrogenation over isolated and nested ≡SiOZn-OH sites grafted onto silanol nests of dealuminated beta zeolite, ACS Catal. 14 (2024) 2787–2804.
[63] Y. Zhang, L. Qi, Y. Li, T. Yang, D.M. Meira, C. Dun, H. Hu, H. Chen, S. Xu, J. J. Urban, A.D. Sadow, T. Kobayashi, L. Qi, P. Tian, A.T. Bell, Mechanism and kinetics of ethanol–acetaldehyde conversion to 1,3-butadiene over isolated lewis acid La sites in silanol nests in dealuminated beta zeolite, ACS Catal. 14 (2024) 15204–15220.
[64] R. Ásmundsson, P. Uvdal, A.D. MacKerell, Binary combination and overtone modes in the C–H stretch region in ethoxy adsorbed on Cu(100): experimental and calculated vibrational spectra, J. Chem. Phys. 113 (2000) 1258–1267.
[65] J. Shan, J. Liu, M. Li, S. Lustig, S. Lee, M. Flytzani-Stephanopoulos, NiCu single atom alloys catalyze the CH bond activation in the selective non- oxidative ethanol dehydrogenation reaction, Appl. Catal. B Environ. 226 (2018) 534–543.
[66] J. Raskó, M. Dömök, K. Baán, A. Erdőhelyi, FTIR and mass spectrometric study of the interaction of ethanol and ethanol–water with oxide-supported platinum catalysts, Appl. Catal. A Gen. 299 (2006) 202–211.
[67] M.I. Zaki, M.A. Hasan, F.A. Al-Sagheer, L. Pasupulety, Surface chemistry of acetone on metal oxides: IR observation of acetone adsorption and consequent surface reactions on silica−alumina versus silica and alumina, Langmuir 16 (2000) 430–436.
[68] V.L. Sushkevich, I.I. Ivanova, E. Taarning, Mechanistic study of ethanol dehydrogenation over silica-supported silver, ChemCatChem 5 (2013) 2367–2373.